Received: 25 September 2026 | Revised: 04 November 2026 | Accepted: 16 November 2026

https://doi.org/10.56946/jce.v5i2.1019
Volume 5 (2): 37-46

Journal of Chemistry and Environment

Research Article

Hydrothermal Synthesis of Porous MoS_2 Nanosheets for Aqueous Electrochemical Capacitors

Tushar Kumar[1], Aditya Singh[1], Madan Lal[1,*], Kuldeep Singh[2], Sahil Dhani[3], Deepak Kumar[1,*]

[1]Department of Physics, Graphic Era Deemed to be University, UK-248002, India.
[2]School of Sciences, Noida International University, Greater Noida, UP-201308, India.
[3]TIET VT CEEM, Thapar Institute of Engineering & Technology, Patiala-147004, India.

*Corresponding authors: (Madan Lal)
madan.physics26@gmail.com ; (Deepak Kumar)
deepakphy@gmail.com

Abstract

Porous MoS_2 nanosheets were synthesized by a hydrothermal method and investigated as electrode materials for aqueous supercapacitors. X-ray diffraction confirmed the formation of crystalline hexagonal MoS_2 with an average crystallite size of approximately 3.12 nm. Scanning electron microscopy revealed a three-dimensional marigold-like assembly of interlinked nanosheets. Nitrogen adsorption-desorption measurements indicated a mesoporous textural structure, with a BET surface area of 4.6962 $m^2\ g^{-1}$, total pore volume of 0.03011 $cm^3\ g^{-1}$, and average pore width of approximately 25.8 nm. The high-relative-pressure hysteresis is consistent with interparticle voids within the nanosheet assembly. Energy-dispersive X-ray spectroscopy confirmed the presence of Mo and S, with no impurity-related elemental signals detected within the measurement sensitivity. Electrochemical performance was evaluated in 1 M KOH using a three-electrode system. Cyclic voltammetry showed Faradaic charge-storage behavior and delivered a specific capacitance of 165.17 F g^{-1} at a scan rate of 10 mV s^{-1}. Galvanostatic charge-discharge measurements yielded a specific capacitance of 110.66 F g^{-1} at 1 A g^{-1}, corresponding to estimated electrode-level gravimetric energy and power densities of 7.53 Wh kg^{-1} and 349.95 W kg^{-1}, respectively. Electrochemical impedance spectroscopy revealed electrolyte and charge-transfer resistances of 4.75 and 1.77 Ω, respectively, indicating favorable ion transport and charge-transfer kinetics. Kinetic analysis indicated a mixed charge-storage mechanism dominated by diffusion-controlled processes, with a smaller surface-controlled contribution. The mesoporous nanosheet assembly, together with the observed electrochemical performance, demonstrates the potential of hydrothermally prepared MoS_2 as an electrode material for aqueous supercapacitors.

Keywords: Electrochemical energy storage; N_2 adsorption-desorption; Brunauer–Emmett–Teller analysis; Electrochemical impedance spectroscopy; diffusion-controlled kinetics.

1. Introduction

The global energy demand is rising, while the conventional fossil-fuel reserves are being depleted. This has increased the demand for an efficient and sustainable energy-storage system. Electrical energy storage systems, in particular supercapacitors, have attracted much attention due to their high-power density, fast charge–discharge rate, long cycle life, and safe operation [1-4].

Supercapacitors are generally classified according to their charge-storage mechanisms into electrical double-layer capacitors (EDLCs) that store charge through ion adsorption at the electrode/electrolyte interface and pseudocapacitors, which utilize fast and reversible Faradaic reactions at or near the surface. The electrochemical performance of supercapacitors is mainly determined by the properties of the electrode material; thus, the development of nanostructured materials with large surface area, abundant electroactive sites, and ideal ion-transport channels is still a major research direction [5-8]. Transition metal chalcogenides, due to their layered architectures, tunable electronic properties, and relatively high theoretical capacitance [9, 10], have emerged as promising electrode materials for energy storage applications. Molybdenum disulfide (MoS_2) has been widely studied owing to its unique two–dimensional layered structure, chemical robustness, and rich redox properties [11-15]. In MoS_2, there is a molybdenum layer sandwiched between two sulfur layers (S–Mo–S), and the neighboring layers are held together by weak van der Waals forces, which allows ion intercalation and diffusion during electrochemical processes [16, 17]. In addition to supercapacitors, MoS_2 has also been investigated for application in lithium-ion batteries, electrocatalysis, photodetectors, and other electronic devices [18].

The electrochemical properties of MoS_2 are influenced by different structural elements (layer thickness, crystallinity, defect density, morphology, etc.) [19, 20]. Porous and nanosheet-based structures are particularly attractive, owing to the presence of short ion–diffusion pathways, enhanced accessibility to electrolytes, and an increased number of electroactive edge sites, which optimize the charge–storage kinetics. Hydrothermal synthesis is an efficient and versatile method for the fabrication of nanostructures, as it allows

morphological regulation under relatively mild conditions and without the need for complex equipment.

Although hydrothermally prepared MoS_2 has been widely investigated for electrochemical energy storage, many reported studies improve its performance through carbonaceous additives, phase engineering, or multicomponent heterostructures [21-27]. The novelty of the present work lies in the preparation and evaluation of a porous, marigold-like MoS_2 nanosheet assembly by a simple hydrothermal route without incorporating additional electroactive materials or a conductive nanocarbon framework into the active material. This approach enables direct investigation of the intrinsic relationship among nanosheet morphology, interparticle mesoporosity, and charge-storage behavior in a single active material MoS_2 electrode. The hydrothermal process provides a straightforward route to interconnected nanosheets with accessible inter-sheet voids, which can facilitate electrolyte penetration, shorten ion-transport pathways, and improve access to electroactive regions. Rather than claiming record capacitance, this study establishes a reproducible baseline for hydrothermally synthesized MoS_2 and clarifies the contribution of its textural architecture to diffusion-controlled charge storage, impedance response, and cycling stability in aqueous KOH electrolyte. Rather than claiming record capacitance, this study establishes a reproducible baseline for hydrothermally synthesized MoS_2 and identifies the contribution of its textural architecture to diffusion-controlled charge storage, impedance response, and cycling stability in aqueous KOH electrolyte. To place the results in context, the performance of the present electrode is compared with representative reported MoS_2 electrodes evaluated in aqueous electrolytes under three-electrode conditions in Section 3.3.5 (Table 3).

2. Materials and methods

2.1. Raw materials

Sodium molybdate dihydrate ($Na_2MoO_4.2H_2O$) and thiourea (NH_2CSNH_2) were purchased from Loba Chemical Pvt. Ltd with 99.9% purity. All the chemicals were of analytical grade and used without further purification. Deionized (DI) water was used throughout the synthesis.

2.2. Synthesis of MoS_2

Porous MoS_2 was synthesized using the hydrothermal method with sodium molybdate dihydrate as the starting precursor. First, 9.68 g of thiourea was dissolved in 50 mL of DI water under constant stirring until a homogeneous solution was obtained. Subsequently, 4.84 g of $Na_2MoO_4.2H_2O$ was added to the solution with continuous stirring for 30 minutes. The resulting solution was then transferred into a 100 mL Teflon–lined stainless-steel autoclave and heated at 180 ℃ for 18 h. Thiourea acted as the sulfur source, while sodium molybdate supplied the molybdenum species required for MoS_2 formation during hydrothermal treatment.

After completion of the reaction, the hot autoclave was allowed to cool naturally to room temperature. The black precipitate was collected by centrifugation and washed 8-9 times with DI water to remove residual ions. After this, the final product was dried at 100 ℃ for 24 h.

2.3. Characterization techniques

The phase purity and crystalline nature of the MoS_2 sample were observed by X–ray diffraction (Model: PANalytical's X'pert Pro) using Cu K_α radiation (λ = 1.5406 Å) with a step size of 0.02° over the 2θ range of 10–80°. The surface morphology and elemental composition were examined using scanning electron microscopy (EVO 18) equipped with energy-dispersive X-ray spectroscopy. The surfaces of the sample were characterized using Oxford Analytical instruments in combination with a Zeiss Sipra 55 field emission electron microscope to determine micrographs, purity, and chemical composition.

Nitrogen adsorption-desorption measurements were carried out at 77 K using a Micromeritics ASAP 2020 surface-area analyzer. Before analysis, the sample was degassed under 10 μmHg at 150 °C for 0.20 h. The BET specific surface area was calculated from the adsorption branch in the relative-pressure range P/P_0 = 0.0557-0.2997. The total pore volume was estimated from the adsorption uptake at P/P_0 = 0.9959. Pore size distribution was determined using the BJH adsorption branch with Harkins-Jura thickness correction. The average pore width was calculated by $4V_P/S_{BET}$, where V_P is the total pore volume, and S_{BET} is the BET specific surface area.

2.4. Electrode preparation and Electrochemical testing

The working electrode was prepared by mixing MoS_2 active material, PVDF, and carbon black in the weight ratio of 80:10:10 using N–methyl–2–pyrrolidone (NMP) as the solvent. The resulting slurry was uniformly coated on a 1 cm x 1 cm graphite sheet and dried at 60 ℃ overnight. The MoS_2 active-material loading was approximately 1 mg cm^{-2}. The specific capacitance values were calculated based on the mass of MoS_2 active material present in the electrode.

The electrochemical measurements were performed in 1 M KOH using a three-electrode configuration, with the MoS_2–modified graphite sheet as the working electrode, a platinum wire as the counter electrode, and an Ag/AgCl electrode as the reference electrode. Cyclic voltammetry (CV), galvanostatic charge–discharge (GCD), and electrochemical impedance spectroscopy (EIS) measurements were carried out using an electrochemical workstation.

The charge-storage properties and capacitance behavior of the electrode were investigated by cyclic voltammetry (CV) at scan rates of 10, 20, 40, 60, 80, and 100 mV s^{-1}, over a potential window of -0.4 to +0.6 V versus Ag/AgCl. The specific capacitance (C_{sp}) was calculated from one CV sweep using the integrated absolute current response, as expressed in Equation (i):

$$C_{sp} = \frac{\int I(V)\,dV}{m\,\nu\,(V_2 - V_1)} (\mathrm{F\ g^{-1}}) \quad \text{..... (i)}$$

where m (1 mg) is the mass of MoS_2 active material, and V_2 (0.6 V) and V_1 (-0.4) are the voltage limits of the potential window.

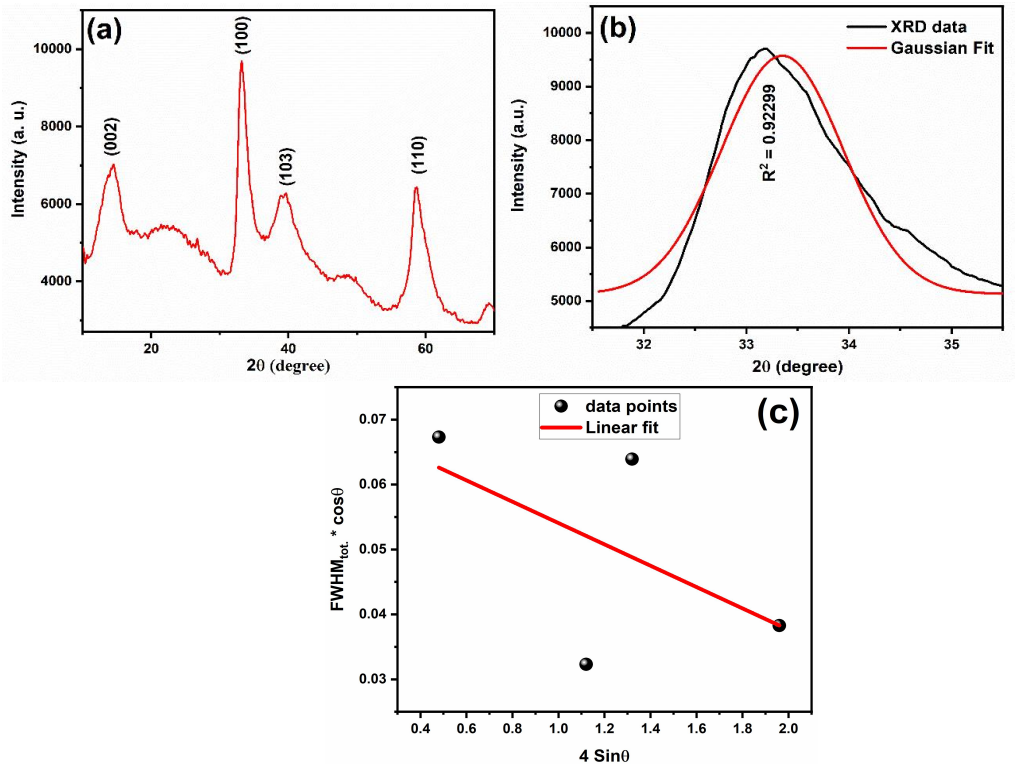

Figure 1. (a) XRD pattern and (b) Gaussian fitting of the (100) diffraction peaks, (c) Williamson-Hall plot of β cosθ versus 4 sinθ, for MoS_2 nanosheets.

Table 1. Various physical parameters calculated for MoS_2 nanosheets.

Plane	2θ (°)	FWHM	d-spacing (nm)	Fitted slope	Goodness of fit (R^2)	Intercept	Crystallite size (nm)	Lattice microstrain (ε)	Dislocation density (nm^{-2})
002	14.42	0.068	0.6416	-0.0164	0.92299	0.0705	2.01	1.6×10^{-2}	2.4×10^{-1}
100	33.13	0.034	0.2750				4.82	2.9×10^{-2}	4.3×10^{-2}
103	39.36	0.068	0.2333				2.14	4.8×10^{-2}	2.1×10^{-1}
110	58.50	0.044	0.1571				3.52	1.9×10^{-2}	8×10^{-2}

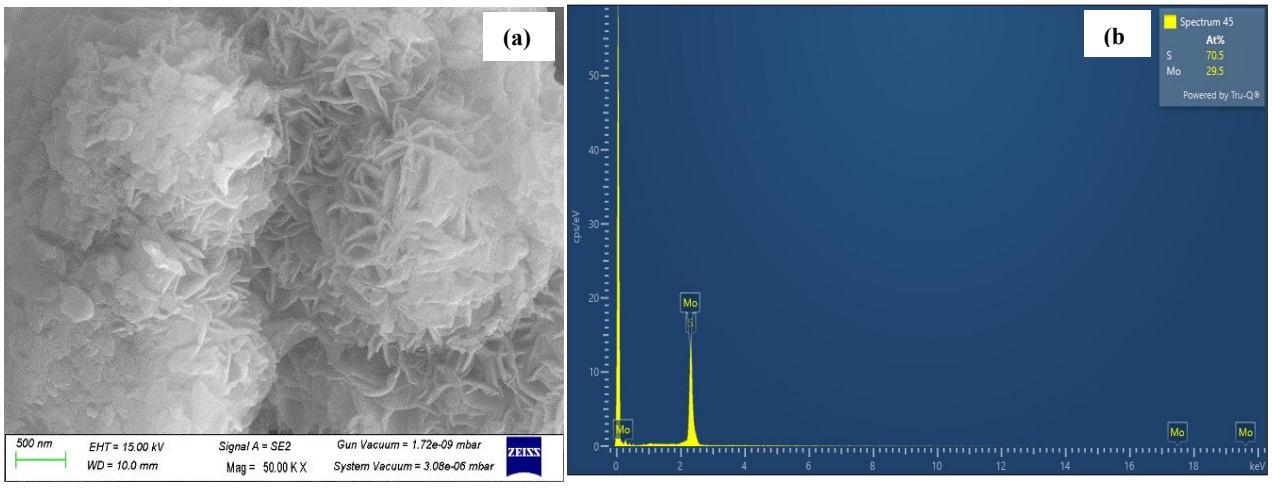

Figure 2. (a) FESEM images and (b) EDX spectra for MoS_2 nanosheets.

The charge-discharge properties, coulombic efficiency, and rate capability of the electrodes were evaluated by galvanostatic charge-discharge (GCD) measurements at current densities of 1, 2, 3, 4, and 5 A g^{-1}, over a potential window of -0.35 to +0.35 V versus Ag/AgCl. The specific capacitance was calculated from the GCD curves according to

Equation (ii):

$$C_{sp} = \frac{I\,\Delta t}{m\,\Delta V}(\mathrm{F\ g^{-1}}) \qquad \text{(ii)}$$

where I is the applied current (A), Δt is the discharge time (s), m is the mass of MoS_2 active material (g), and ΔV is the full discharge potential window of 0.70 V used for calculation (the initial IR drop was included in it).

In addition, the GCD data were used to calculate the electrode-level gravimetric energy density (E_d) and gravimetric power density (P_d) according to Equations (iii) and (iv), respectively.

$$E_d \frac{C_{sp} \times (\Delta V)^2}{7.2} \qquad \text{(iii)}$$

$$P_d = \frac{3600 * E_d}{\Delta t}(\mathrm{W\ kg^{-1}}) \qquad \text{(iv)}$$

Electrochemical impedance spectroscopy (EIS) was measured over the frequency range of 100 kHz to 0.01 Hz to investigate the charge transfer resistance, ion diffusion properties, and the overall electrochemical kinetics of the electrodes. Further analysis of the impedance data was carried out by means of suitable equivalent circuit models to obtain quantitative parameters such as solution resistance, charge transfer resistance, and constant phase element parameters.

3. Results and discussion

3.1. X-ray diffraction analysis

The X-ray diffraction analysis (Figure 1a) was performed to evaluate the crystal structure and phase purity of the hydrothermally synthesized MoS_2 sample. The diffraction peaks observed at 2θ angles of about 14.42°, 33.13°, 39.36°, and 58.50° correspond to the (002), (100), (103), and (110) crystallographic planes of hexagonal MoS_2, respectively, which agree with the standard JCPDS data 37-1492 for hexagonal 2H–MoS_2. The absence of additional diffraction peaks indicates that no detectable crystalline impurity phases were observed above the detection limit of the instrument, confirming the phase purity of the synthesized sample.

The average crystallite size was estimated from the broadening of the X-ray diffraction (XRD) peaks using the Scherrer equation (Equation v):

$$D = k\,\lambda / (\beta \cos\theta) \qquad \text{(v)}$$

Where D is the crystallite size, k is the shape factor (0.9), λ is the X-ray wavelength (1.5406 Å), β is the full width at half maximum (FWHM) of the diffraction peak in radians, and θ is the Bragg angle. The calculated average crystallite size of the synthesized MoS_2 was approximately 3.12 nm, confirming the nanocrystalline nature of the material. The observed peak broadening is therefore consistent with the small crystallite size of the synthesized MoS_2.

The Gaussian fitting of the (100) diffraction peaks, shown in Figure 1b, was used to determine the corresponding FWHM more accurately. To further examine the contributions of crystallite size and lattice strain to the XRD peak broadening, the Williamson-Hall (W-H) method was employed using the uniform deformation model. TThe W–H relationship is expressed as Equation (v):

$$\beta \cos\theta = \frac{k\,\lambda}{D} + 4\varepsilon \sin\theta \qquad \text{(v)}$$

Where β is the instrument-corrected full-width, and ε is the lattice microstrain. Accordingly, β cosθ was plotted against 4 sinθ as shown in Figure 1c. The linear fitting of the experimental data allows crystallite size and microstrain to be estimated from the intercept and slope, respectively. The intercept provides the average crystallite size, whereas the slope corresponds to microstrain. The fitting parameters are listed in Table 1.

The Williamson-Hall plot showed poor linearity, indicating that the available diffraction peaks do not allow a reliable separation of size and strain broadening using the uniform deformation model. Therefore, no quantitative W-H microstrain value was interpreted in this work. Crystallite size, lattice strain, and dislocation density (Table 1) were calculated using the Scherrer equation from the instrument-corrected peak widths.

The XRD results confirm the formation of single–phase hexagonal MoS_2 within the detection limit of XRD. The small crystallite size and layered crystal structure may be beneficial for electrochemical charge storage by providing short ion–diffusion pathways and potentially improving accessibility of electroactive regions.

3.2. Morphological and chemical analysis

The surface morphology of the hydrothermally synthesized MoS_2 sample was studied by scanning electron microscopy (SEM), and the corresponding micrographs are shown in Figure 2a. SEM images show a 3-D marigold–like structure formed by interconnected nanosheets. The nanosheets are laterally clustered to form a porous structure with thicknesses below ~50 nm.

The permeable and interconnected nanosheet architecture may facilitate electrolyte penetration and improve the accessibility of electroactive regions. In addition, the nanoscale thickness of the sheets may reduce characteristic ion–diffusion distances and enhance electroactive-site utilization during the charge–discharge cycles. Such morphological features are generally favorable for electrochemical charge–storage performance in the supercapacitor electrodes [24].

The observed marigold–like structure may be associated with the hydrothermal growth method, where thiourea is the sulfur source and sodium molybdate provides molybdenum species. The observed morphology may result from anisotropic growth and self-assembly of MoS_2 nanosheets during the hydrothermal process. The resulting structure contains numerous inter-sheet voids and interconnected channels, which may facilitate electrolyte accessibility.

The elemental makeup of the produced sample was analyzed by energy-dispersive X-ray spectroscopy (EDX), as depicted in Figure 2(b). The EDX spectrum confirms the presence of Mo and S, with no detectable impurity–related elemental signals within the sensitivity of the measurement.

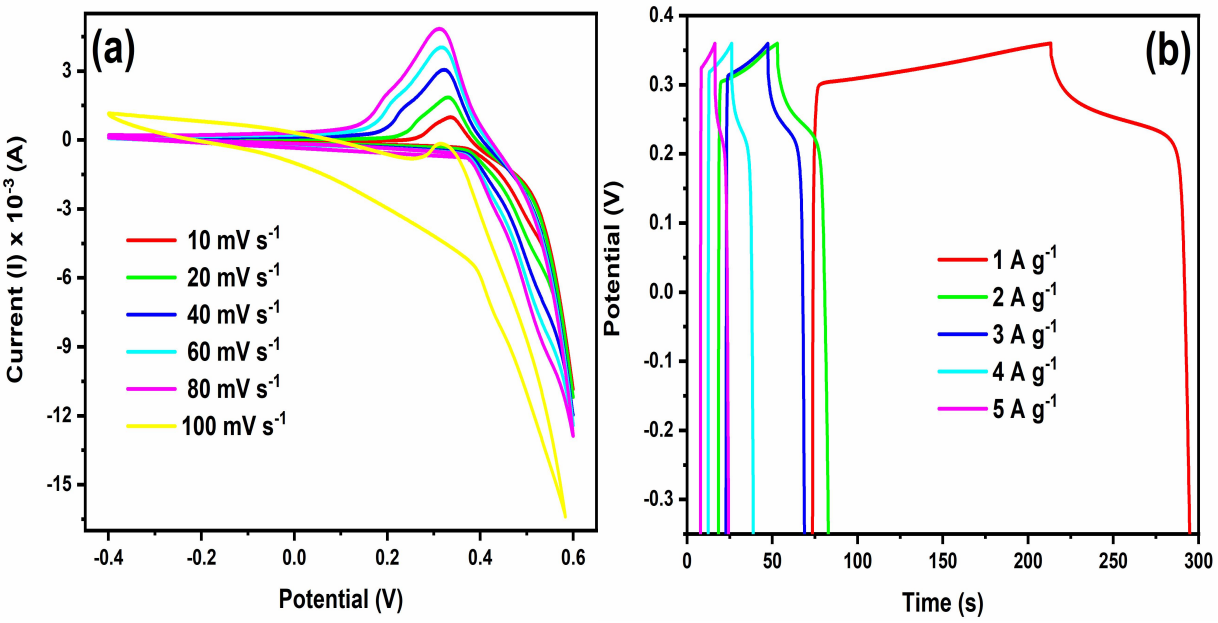

Figure 3. (a) CV curves at different scan rates and (b) GCD curves for MoS_2 nanosheets.

Table 2. GCD-derived specific capacitance and estimated electrode-level gravimetric energy and power of the MoS_2 electrode in a three-electrode configuration.

Current Density (A g^{-1})	Galvanostatic Charge-Discharge		
	C_{sp} (F g^{-1})	E_d (Wh kg^{-1})	P_d (W kg^{-1})
1	110.66	7.53	349.95
2	80	5.44	699.43
3	85.6	5.83	1050.80
4	67.73	4.61	1400.18
5	53.33	3.63	1750.29

Table 3. Comparison of the electrochemical performance of the present MoS_2 electrodes with selected reported MoS_2 -based electrodes.

Electrode material	Preparation method	Electrolyte/ configuration	Specific capacitance	Cycling retention	Ref.
MoS_2 nanosheet assembly	Hydrothermal, 180 °C, 18 h	1 M KOH/three-electrode	110.66 F g^{-1} at 1 A g^{-1} (GCD)	99.4% after 4000 cycles	This work
Flower-like MoS_2 microspheres (MoS_2-16)	Hydrothermal, 200 °C, 16 h	1 M Na_2SO_4/three-electrode	518.7 F g^{-1} at 1 A g^{-1} (GCD)	88.2% after 2500 cycles	[28]
MoS_2 nanoflowers	Gelatin-assisted hydrothermal synthesis, 220 °C, 24 h	1 M Na_2SO_4/three-electrode	220 F g^{-1} at 1 A g^{-1} (GCD)	97% after 2250 cycles at 4 A g^{-1}	[29]
2H-MoS_2 nanosheets	One-step-hydrothermal method, 180 °C, 24 h	1 M Na_2SO_3/three-electrode	143.12 F g^{-1} at 1 A g^{-1} (GCD)	87.1% after 5000 cycles at 1 A g^{-1}	[30]
Flower-like MoS_2 nanostructures	Two-step hydrothermal method	1 M Na_2SO_3/three-electrode	168 F g^{-1} at 1 A g^{-1} (GCD)	92.6% after 3000 cycles	[31]
MoS_2 nanosheets	Topochemical sulfurization	Aqueous/three-electrode	119.38 F g^{-1} 1 A g^{-1} (CV)	95.1% after 2000 cycles	[32]
MoS_2 quantum dots (~2 nm)	Laser-assisted chemical-vapour deposition	1 M KCl/three-electrode	255 F g^{-1} at 1 mV s^{-1} (CV)	NR for the three-electrode test	[33]

The SEM and EDX analyses confirm the successful formation of porous MoS_2 nanosheets with a hierarchical flower–like morphology and the presence of Mo and S without detectable impurity–related elemental signals. The observed nanosheet architecture and inter-sheet voids may facilitate electrolyte accessibility and contribute to electrochemical charge-storage behavior.

3.3. Electrochemical analysis

The electrochemical properties of the hydrothermally synthesized MoS_2 electrode were examined in 1 M KOH using a three–electrode system configuration. Cyclic voltammetry (CV), galvanostatic charge–discharge (GCD), and electrochemical impedance spectroscopy (EIS) were carried out using an electrochemical workstation.

3.3.1. Cyclic voltammetry

The cyclic voltammetry measurements were conducted over a potential window of −0.4 to +0.6 V versus Ag/AgCl at different scan rates (Figure 3a). The CV profiles exhibit pronounced Faradaic redox reactions, indicating substantial contribution from Faradaic charge-storage processes. The subsequent kinetic analysis shows that the overall electrochemical response is a combination of diffusion–controlled and surface–controlled contributions, where the diffusion–controlled part dominates.

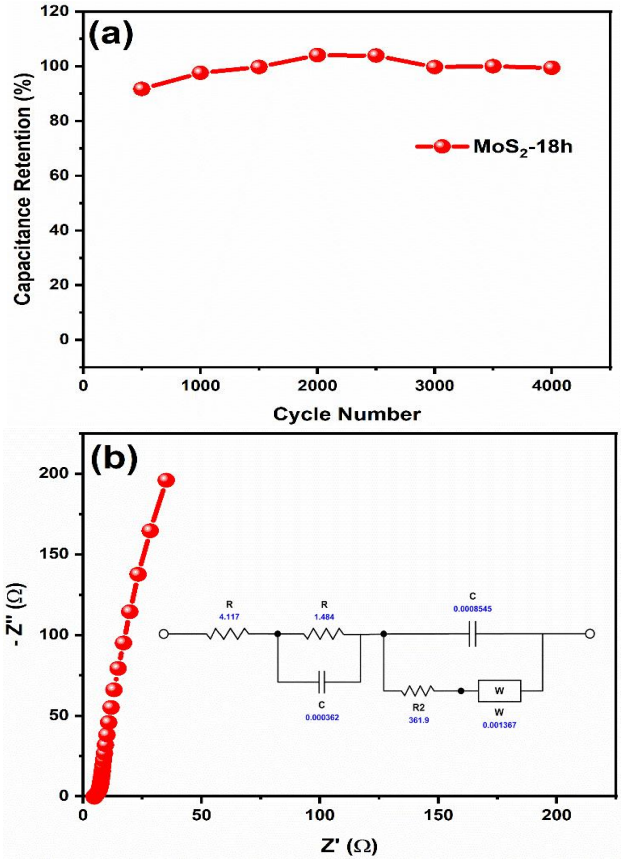

Figure 4. (a) Cyclic stability and (b) Nyquist plots for MoS_2 nanosheets.

The decrease in capacitance at high scan rates can be explained by the limited diffusion of electrolyte ions inside the inner pores and the reduced effectiveness of the electroactive site utilization at fast potential changes [19, 22]. At small scan rates, electrolyte ions have enough time to diffuse into the porous structure of the nanosheets, leading to higher charge–storage utilization. The CV measurements showed a maximum specific capacitance of 165.17 F g^{-1} at a scan rate of 10 mV s^{-1}. The specific capacitance decreased with an increase in scan rate, indicating limited participation of electroactive sites at higher scan rates. Energy and power densities were determined by galvanostatic charge-discharge evaluations, as described in the next section.

3.3.2. Galvanostatic charge-discharge analysis

Figure 3b shows that the GCD measurements were conducted over a potential window of -0.35 to +0.35 V versus Ag/AgCl. The charge-discharge curves show an almost triangular symmetry with slight deviation from linearity, consistent with mixed charge-storage processes. As expected, the discharge time generally decreased with increasing current density because higher currents provide less time for electrolyte ions to access the regions of the electrode.

The specific capacitance reached 110.66 F g^{-1} at a current density of 1 A g^{-1} over the potential window of -0.35 to +0.35 V. The estimated electrode-level energy and power densities were 7.53 Wh kg^{-1} and 349.95 W kg^{-1}, respectively, as listed in Table 2. Overall, the specific capacitance exhibited a decreasing trend with increasing current density, decreasing from 110.66 F g^{-1} at 1 A g^{-1} to 53.33 F g^{-1} at 5 A g^{-1}. A minor deviation from a strictly monotonic trend was observed at 3 A g^{-1}, where the calculated specific capacitance was slightly higher than that at 2 A g^{-1}. This variation may be associated with differences in electrolyte wetting and the accessibility of electroactive sites during the charge-discharge process. Therefore, the overall reduction in capacitance at higher current densities may be attributed to diffusion limitations and polarization effects, which restrict ion transport and limit access to electrochemically active regions within the porous electrode.

3.3.3. Cycling stability

The cycling stability of the MoS_2 electrode was evaluated at a scan rate of 150 mV s^{-1} over a potential window of -0.5 to +0.5 V versus Ag/AgCl. The capacitance retention was calculated using the equation $C_n/C_1 \times 100$, where C_1 and C_n are the specific capacitances for the first and n^{th} cycles, respectively. The coulombic efficiency was calculated as the ratio of discharge time to charge time multiplied by 100. The recorded coulombic efficiencies are 94.11, 92, 86.17, 86.45, and 58.69% at current densities of 5, 4, 3, 2, and 1 A g^{-1}, respectively.

Figure 4a shows that an initial increase in the capacitance retention was observed during the early cycles, followed by a gradual decrease after 2500 cycles and subsequent stabilization over prolonged cycling. This behavior may be associated with progressive electrolyte wetting of the porous electrode and gradual activation of previously inaccessible electroactive sites during repeated charge-discharge cycling. As these mechanisms were not directly investigated, this interpretation should be considered tentative. Nevertheless, the electrode exhibited good electrochemical stability under the applied testing conditions, retaining approximately 99.4% of its capacitance after 4000 cycles (using first/4000th cycle CV curves).

Table 4. Surface and pore-textural characteristics of the MoS_2 nanosheets from N_2 adsorption-desorption analysis.

Sample	Surface area ($m^2\ g^{-1}$)	V-t method surface area ($m^2\ g^{-1}$)	Langmuir surface area ($m^2\ g^{-1}$)	BJH surface area ($m^2\ g^{-1}$)	BJH pore volume ($cm^3\ g^{-1}$)
MoS_2	4.6962	5.3121	4.6956	4.6710	0.03011

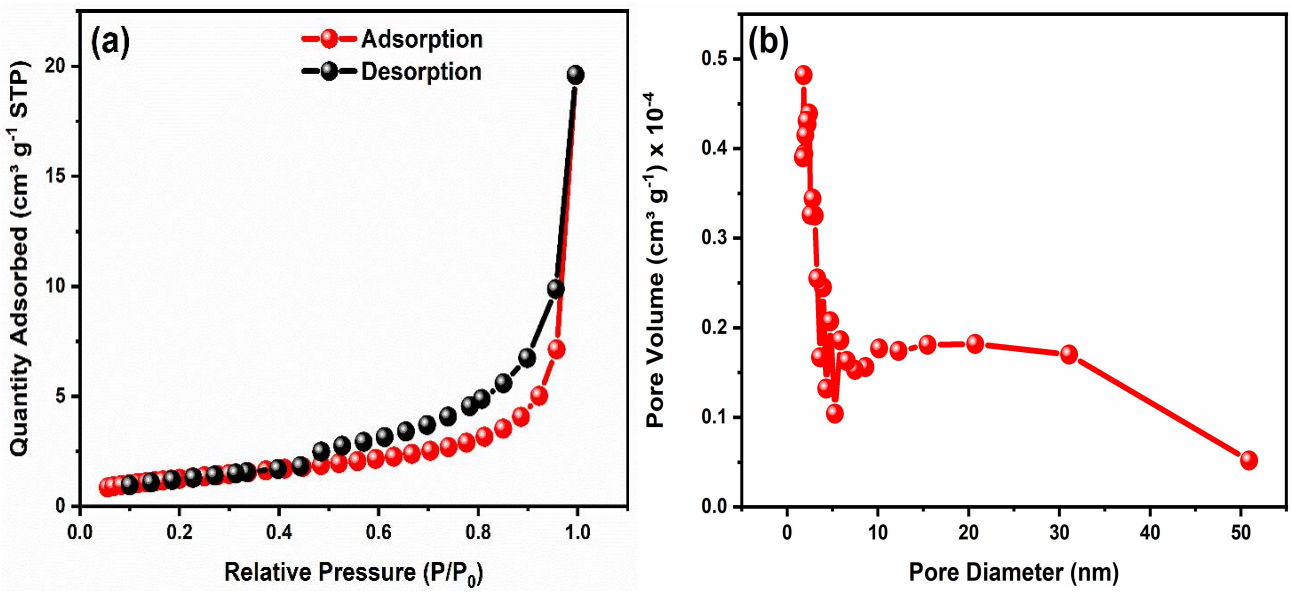

Figure 5. (a) N_2 adsorption-desorption isotherms and (b) BJH adsorption pore-size distribution for MoS_2 nanosheets.

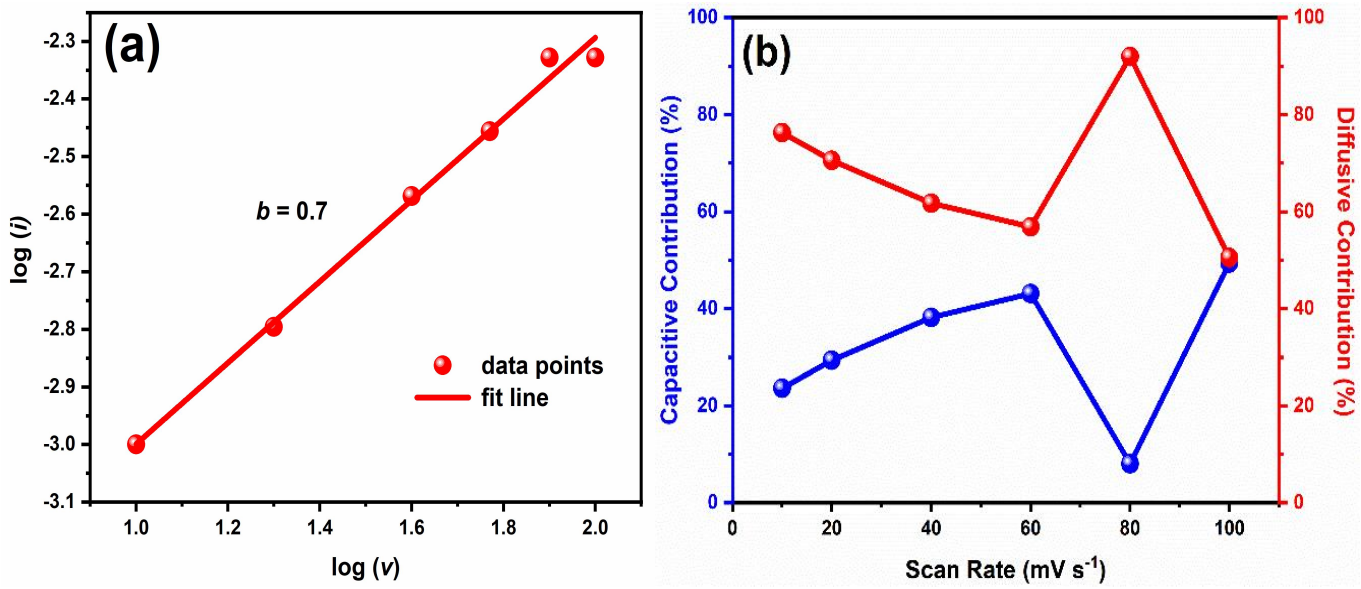

Figure 6. (a) Power law dependence of peak current at different scan rates, and (b) capacitive and diffusion-controlled contributions as a function of scan rate, for MoS_2 nanosheets.

3.3.4. Electrochemical impedance spectroscopy

Electrochemical impedance spectroscopy (EIS) measurements were performed in the frequency range of 0.01 Hz to 100 kHz, and the Nyquist plot is presented in Figure 4(b). The high-frequency intercept on the real axis is assigned to the electrolyte resistance (R_S), and the semicircle at the medium frequency is related to the charge transfer resistance (R_{ct}). The obtained R_s = 4.75 Ω and R_{ct} = 1.77 Ω values indicate relatively low ohmic and favorable charge-transfer properties.

The near-vertical low-frequency response is consistent with predominantly capacitive behavior and favorable ion transport under the measurement conditions. The corresponding Bode plot shows a phase angle close to 90° at low frequencies, consistent with the capacitive nature of the electrode, although some deviations from the ideal behavior are expected due to the Faradaic charge–transfer processes.

3.3.5. Comparison with reported MoS_2-electrodes

To place the electrochemical performance of the current electrode in context, it was compared with recently reported undoped MoS_2 electrodes evaluated in aqueous three-electrode configurations, as summarized in Table 3. The MoS_2 nanosheet assembly delivered a specific capacitance of 110.66 F g^{-1} at 1 A g^{-1} in 1 M KOH, which is lower than values reported for flower-like MoS_2 microspheres and MoS_2 nanoflowers in a 1 M Na_2SO_4 electrolyte [28, 29]. However, direct comparison of capacitance values should be made with caution due to the differences in electrolyte, electrode substrate, active-material loading, potential window, and measurement protocols among studies.

The present electrode exhibited a charge-transfer resistance of 1.77 Ω and retained 99.4% of the initial capacitance after 4000 cycles, indicating favorable charge-transfer characteristics and cycling stability. Although the hydrothermally synthesized MoS_2 nanosheets do not exhibit record capacitance, their interconnected nanosheet architecture and accessible interparticle voids contribute to the stable electrochemical performance in aqueous KOH electrolyte.

The porous and textural properties of the MoS_2 sample were examined by N_2 adsorption-desorption analysis. The isotherm displays a pronounced adsorption-desorption hysteresis loop, particularly at high relative pressure (P/P_0), together with a steep uptake near P/P_0 = 0.9-1.0 (Figure 5a). This behavior is consistent with mesoporous textural features and interparticle voids formed by the assembly of nanosheets. The high-pressure uptake should primarily be associated with capillary condensation in larger mesopores and textural voids rather than a uniform intrinsic pore network.

The BET specific surface area of the sample was 4.6962 m^2 g^{-1}, while the total pore volume was 0.03011 cm^3 g^{-1}. The corresponding average pore width was approximately 25.8 nm, placing the average pore size within the mesoporous range. These results indicate that the sample possesses a mesoporous texture with modest surface area and pore volume. Such a structure can facilitate electrolyte penetration and shorten ion-diffusion pathways in the electrode. All the parameters are listed in Table 4.

The BJH pore-size distribution was calculated using the Harkins-Jura thickness correction. Figure 5b shows that the distribution has its highest contribution in the small-mesopore region, approximately 2-4 nm, followed by a broad tail extending to about 50.9 nm. Thus, 50.9 nm should be regarded as the upper range of the observed pore-size distribution rather than the pore diameter with the maximum pore-volume contribution. The BJH cumulative pore volume of 0.03011 cm^3 g^{-1} agrees well with the total pore volume obtained from the adsorption isotherm. Overall, the BET and BJH results support the presence of a mesoporous nanosheet assembly containing both smaller mesopores and larger interparticle voids. Although the surface area is modest, this porous texture may improve electrolyte accessibility and contribute to ion transport during electrochemical charge storage.

To further understand the charge storage mechanism, the power law correlation between the peak current (i) and the scan rate (v) was used:

$$i = av^b \qquad (vii)$$

where a and b are adjustable parameters. From Figure 6a (i.e., the log(i) vs log(v) plot), the gradient gave a b–value of about 0.7, which indicated a hybrid charge-storage mechanism involving both diffusion-controlled and surface–controlled processes [34]. The capacitive and diffusion–controlled parts were separated by the method of Dunn:

$$i(V) = k_1v + k_2v^{1/2} \qquad (viii)$$

where k_1v is the surface–controlled contribution, whereas $k_2v^{1/2}$ represents the diffusion–controlled contribution [35].

At a scan rate of 80 mV s^{-1}, the diffusion–controlled contribution accounted for ~ 86.2%, whereas the surface–controlled contribution accounted for about 13.8%, as shown in Figure 6b. These results indicate a mixed charge-storage mechanism involving both diffusion-controlled and surface–controlled processes, with the diffusion–controlled contribution dominating under the investigated conditions.

The electrochemical studies indicate mixed Faradaic charge-storage behavior, moderate specific capacitance, low charge-transfer resistance, and good cycling stability of the porous MoS_2 nanosheet electrode.

4. Conclusion

Porous MoS_2 nanosheets were successfully synthesized by a hydrothermal process at 180 °C for 18 h. X-ray diffraction confirmed the formation of nanocrystalline hexagonal MoS_2, while SEM revealed a hierarchical marigold-like architecture composed of interconnected nanosheets and inter-sheet voids. EDX confirmed the presence of Mo and S, with no impurity-related elemental signals detected within the sensitivity of the measurement. N_2 adsorption-desorption analysis further verified the mesoporous textural character of the material, giving a BET surface area of 4.6962 m^2 g^{-1}, a total pore volume of 0.03011 cm^3 g^{-1}, and an average pore width of approximately 25.8 nm. The hysteresis observed at high relative pressure is consistent with interparticle voids within the nanosheet assembly.

Electrochemical measurements in aqueous KOH demonstrated mixed Faradaic charge-storage behavior. The electrode delivered a specific capacitance of 165.17 F g^{-1} at a scan rate of 10 mV s^{-1} from cyclic voltammetry and 110.66 F g^{-1} at a current density of 1 A g^{-1} from galvanostatic charge-discharge measurements. Electrochemical impedance spectroscopy showed relatively small electrolyte and charge-transfer resistances (R_S = 4.75 Ω and R_{ct} = 1.77 Ω), indicating

favorable ion transport and charge-transfer characteristics under the tested conditions. The electrode retained 99.4% of its initial capacitance after 4000 cycles, demonstrating good cycling stability.

Kinetic analysis gave a *b*-value of approximately 0.7, indicating a hybrid charge-storage mechanism involving both diffusion-controlled and surface-controlled processes. The mesoporous nanosheet assembly, modest surface area and pore volume, accessible electroactive sites, and stable electrochemical response indicate that hydrothermally synthesized MoS_2 is a promising electrode material for aqueous supercapacitor applications. These findings provide a basis for further optimization of electrode architecture and evaluation of MoS_2-based systems in practical two-electrode configurations.

5. Future Research Scope

Future studies should focus on the systematic optimization of the hydrothermal synthesis parameters, such as reaction time, temperature, precursor ratios, and post-processing, to understand the relationships between the MoS_2 crystallinity, defect density, nanosheet organization, pore accessibility, and electrochemical performance. The limited BET surface area and interparticle mesoporous structure can be improved for enhanced electrolyte accessibility and active-site utilization. Future work should also investigate the effects of increasing active-material loading, conductive substrates, and proper carbon or metal-oxide hybridization on the rate capability and the charge-transfer resistance. Additional mechanistic information from in situ/operando characterization and structural/compositional analysis after cycling would clarify the mechanisms of charge storage dominated by Faradaic and diffusion processes. Finally, the material should be evaluated in practical two-electrode symmetric or asymmetric supercapacitor architectures considering device-level energy and power density, coulombic efficiency, self-discharge, leakage current, and long-term cycling stability under real operating conditions.

Author contributions

Tushar Kumar: Methodology, Writing-original draft, data curation, Writing-review & editing. Aditya Singh: Methodology, Writing-original draft. Madan Lal: Data curation, Conceptualization, Validation, formal analysis, supervision, Writing-review & editing. Kuldeep Singh: Writing-review & editing. Sahil Dani: Writing-review & editing. Deepak Kumar: Data curation, Conceptualization, Validation, formal analysis, supervision, Writing-review & editing. All authors have read and agreed to the published version of the manuscript.

Ethical approval

Not applicable.

Conflicts of Interest

The authors report no conflicts of interest.

Acknowledgment

The authors would like to thank the Honourable Vice-Chancellor, Prof. (Dr.) Narpinder Singh, and Dean Projects, Prof. (Dr.) Pardeep Sharma, Graphic Era Deemed to be University, for providing seed money for the project entitled “Development of Chalcogenide and Perovskite Composites for Supercapacitor Applications.

Data availability statement

The data that support the findings of this study are available on request from the corresponding authors.

Funding

Not Applicable (N/A).

Declaration of generative AI use

During the preparation of this work, the author(s) used an AI-assisted language tool (ChatGPT 5.2, OpenAI) to improve the manuscript’s clarity and readability. The author(s) have reviewed and edited the content as necessary and take full responsibility for the content of the published article.

REFERENCES

1. Winter, M. and R.J. Brodd, What are batteries, fuel cells, and supercapacitors? Chemical reviews, 2004. 104(10): p. 4245–4270.
2. Zhang, L.L. and X. Zhao, Carbon-based materials as supercapacitor electrodes. Chemical society reviews, 2009. 38(9): p. 2520–2531.
3. Simon, P. and Y. Gogotsi, Materials for electrochemical capacitors. Nature materials, 2008. 7(11): p. 845–854.
4. Sharma, N., et al., Harnessing Nature-Derived Sustainable Materials for Electrochemical Energy Storage: Unveiling the Mechanism and Applications. Macromolecular Materials and Engineering, 2025. 310(1): p. 2400129.
5. Theerthagiri, J., et al., Recent advances in metal chalcogenides (MX; X= S, Se) nanostructures for electrochemical supercapacitor applications: a brief review. Nanomaterials, 2018. 8(4): p. 256.
6. Muller, G.A., et al., High performance pseudocapacitor based on 2D layered metal chalcogenide nanocrystals. Nano letters, 2015. 15(3): p. 1911–1917.
7. Zhang, Y., et al., Two-dimensional transition metal chalcogenides for alkali metal ions storage. ChemSusChem, 2020. 13(6): p. 1114–1154.
8. Lv, T., et al., Co-intercalation of dual charge carriers in metal-ion-confining layered vanadium oxide nanobelts for aqueous zinc-ion batteries. Angewandte Chemie, 2023. 135(5): p. e202216089.
9. Gao, M.-R., et al., Nanostructured metal chalcogenides: synthesis, modification, and applications in energy conversion and storage devices. Chemical Society Reviews, 2013. 42(7): p. 2986–3017.
10. Zhang, Y., et al., Nanostructured metal chalcogenides for energy storage and electrocatalysis. Advanced Functional Materials, 2017. 27(35): p. 1702317.
11. Yin, Z., et al., Single-layer MoS2 phototransistors. ACS nano, 2012. 6(1): p. 74–80.

12. Lee, H.S., et al., MoS2 nanosheet phototransistors with thickness-modulated optical energy gap. Nano letters, 2012. 12(7): p. 3695–3700.
13. Xiao, J., et al., Exfoliated MoS2 nanocomposite as an anode material for lithium ion batteries. Chemistry of Materials, 2010. 22(16): p. 4522–4524.
14. Huang, K.-J., et al., Layered MoS2–graphene composites for supercapacitor applications with enhanced capacitive performance. International journal of hydrogen energy, 2013. 38(32): p. 14027–14034.
15. Thangappan, R., et al., Graphene decorated with MoS 2 nanosheets: a synergetic energy storage composite electrode for supercapacitor applications. Dalton transactions, 2016. 45(6): p. 2637–2646.
16. Verble, J. and T. Wieting, Lattice mode degeneracy in MoS2 and other layer compounds. Physical review letters, 1970. 25(6): p. 362.
17. Van Schalkwijk, W. and B. Scrosati, Advances in lithium ion batteries introduction, in Advances in lithium-ion batteries. 2002, Springer. p. 1–5.
18. Zhang, X., et al., Hydrothermal synthesis and characterization of ultrathin MoS2 nanosheets. Chalcogenide letters, 2016. 13(1).
19. Yang, Y., et al., Edge-oriented MoS2 nanoporous films as flexible electrodes for hydrogen evolution reactions and supercapacitor devices. Advanced materials, 2014. 26(48): p. 8163–8168.
20. Jiang, L., et al., Optimizing hybridization of 1T and 2H phases in MoS2 monolayers to improve capacitances of supercapacitors. Materials Research Letters, 2015. 3(4): p. 177–183.
21. Raikwar, A.S. and H.S. Panda, A review on nano-structured electrodes for high-performance supercapacitors: panoramic insights across dimensional spectra. Discover Electronics, 2025. 2(1): p. 94.
22. Krishnamoorthy, K., et al., Mechanically delaminated few layered MoS2 nanosheets based high performance wire type solid-state symmetric supercapacitors. Journal of Power Sources, 2016. 321: p. 112–119.
23. Gopalakrishnan, K., et al., Performance of MoS2-reduced graphene oxide nanocomposites in supercapacitors and in oxygen reduction reaction. Nanomaterials and Energy, 2015. 4(1): p. 9–17.
24. Rani, S., et al., Engineered nano-architecture for enhanced energy storage capabilities of MoS2/CNT-heterostructures: A potential supercapacitor electrode. Journal of Energy Storage, 2024. 84: p. 110865.
25. Raghav, J., et al., Recent advances in electrode materials for high-performance supercapacitor applications. Journal of Energy Storage, 2026. 146: p. 120016.
26. Du, X., et al., Electrode materials, structural design, and storage mechanisms in hybrid supercapacitors. Molecules, 2023. 28(17): p. 6432.
27. Nassar, K.I., L. Pereira, and M. Graça, Perovskite Materials: Crystal Chemistry, Synthesis, and Selected Functional Applications. Crystals, 2026. 16(11): p. 702.
28. Wang, F., et al., Hydrothermal synthesis of flower-like molybdenum disulfide microspheres and their application in electrochemical supercapacitors. RSC advances, 2018. 8(68): p. 38945–38954.
29. Yang, Q., et al., Hydrothermal synthesis of MoS2 nanoflowers and their capacitive property. Micro & Nano Letters, 2019. 14(5): p. 493–495.
30. Wang, H., X. Xu, and A. Neville, Facile synthesis of vacancy-induced 2H-MoS2 nanosheets and defect investigation for supercapacitor application. RSC advances, 2021. 11(42): p. 26273–26283.
31. Wang, X., et al., High supercapacitor and adsorption behaviors of flower-like MoS2 nanostructures. Journal of Materials Chemistry A, 2014. 2(38): p. 15958–15963.
32. Kesavan, D., et al., Topochemically synthesized MoS2 nanosheets: a high performance electrode for wide-temperature tolerant aqueous supercapacitors. Journal of Colloid and Interface Science, 2021. 584: p. 714–722.
33. Panchu, S.J., et al., Luminescent MoS2 quantum dots with tunable operating potential for energy-enhanced aqueous supercapacitors. ACS omega, 2021. 6(7): p. 4542.
34. Wang, R., et al., Elucidating the intercalation pseudocapacitance mechanism of MoS2–carbon monolayer interoverlapped superstructure: toward high-performance sodium-ion-based hybrid supercapacitor. ACS applied materials & interfaces, 2017. 9(38): p. 32745–32755.
35. Choudhary, N., et al., Asymmetric supercapacitor electrodes and devices. Advanced Materials, 2017. 29(21): p. 1605336.

Copyright © 2026 by the author(s).
Published by Science Research Publishers.
This article is an open-access article distributed under the terms and conditions of the Creative Commons Attribution-Non-Commercial-No Derivatives (CC BY-NC-ND 4.0)

How to cite this article:
Kumar, T., Singh, A., Lal, M., Singh, K., Dhani, S., & Kumar, D. (2026). Hydrothermal Synthesis of Porous MoS_2 Nanosheets for Aqueous Electrochemical Capacitors. Journal of Chemistry and Environment, 5(2), 37-46.